Indian Journal of Chemistry
Vol. 63, August 2024, pp. 797-806
DOI: 10.56042/ijc.v63i8.10078

Heat dissipating multi-component inorganic mixture of iron with high-temperature dielectric behaviour

Gouri Sankhar Brahma[a], Akash Kumar Sahu[a] & Suprava Nayak*[b]

[a] Faculty of Science and Technology, IFHE, Hyderabad 501 203, Telangana, India

[b] School of Chemistry, Gangadhar Meher University, Sambalpur 768 004, Odisha, India

E-mail: suprava7107@gmail.com

Received 2 April 2024; accepted (revised) 2 August 2024

Synthesis and characterization of two multicomponent mixtures, 0.8 $Fe_3(PO_4)_2{\cdot}4H_2O$ · 0.8 $FePO_4$ · $2H_2O$ · 0.5 $NH_4H_2PO_4$ · $0.2(NH_4)_2SO_4$ (**FPN2A**) and 0.8 $Fe_3(PO_4)_2$ ·$8H_2O$· $0.8FePO_4$· $0.5NH_4H_2PO_4{\cdot}0.2(NH_4)_2SO_4$ (**FPN2B**) are reported. FPN2A and FPN2B mixtures have average crystallite sizes of 66.1 nm and 79.5 nm, respectively. The respective optical bandgap of FPN2A and FPN2B are 6.02 eV and 5.96 eV with a refractive index of 1.99. Thermal analysis reveals heat-dissipating behaviour of the mixtures with specific heat capacity, C_P (at 307K) of 0.71 $Jg^{-1}K^{-1}$ and 0.66 $Jg^{-1}K^{-1}$ for FPN2A and FPN2B, respectively. Further, temperature-frequency dependant dielectric properties of the FPN2C (obtained by sintering FPN2B at 423K) have been investigated. The sintered mixture, FPN2C orchestrated variation in permittivity, ϵ' (~17 – 42) and dielectric loss, tan δ (~0.04-0.08) in the frequency range of 1.0×10^3 Hz to 4.0×10^6 Hz up to 483K. AC conductivity of FPN2C has been found to be ~ 8.96×10^{-8} sm^{-1} up to 483K. TG-DSC analysis reveals the thermal stability of the FPN2C over a wide range of temperature (297K to 1267K) and heat-dissipating behaviour with a C_P of 0.62 $Jg^{-1}K^{-1}$.

Keywords: Heat dissipation, Specific heat capacity, Dielectric properties, AC conductivity

Human race thrive with the development of advanced technologies. As the standard of living rises, so does their energy demand. As the world's energy demand increases, efficient energy storage, and utilisation become more important. Energy storage has become a critical aspect for the proper implementation of generated energy from immutable and artificial sources to maintain the ecological society's sustainable development and reduce anthropogenic alterations[1]. For the storage of electrical energy, supercapacitor, fuel cells, dielectric capacitors, batteries are proven to be promising devices[2-9]. Among all, dielectric materials in particular are gaining popularity due to their rapid charging-discharging rate, which is achieved through dielectric polarisation and depolarisation in response to an external electric field, rather than a chemical reaction [10-13]. Several polymer dielectrics have been studied widely as energy harvesting sources[14,15], transducers[16-18], soft robots[19-23], printable electronics[24], energy storage devices[25]. Although polymer dielectrics have higher breakdown strength and reliability, they are restricted to low operational temperatures and so cannot fulfill the growing demand for energy[3]. Many efforts have been made to increase the energy density on dielectric materials like lead lanthanum zirconate lead magnesium niobate, lead tantanate, since they deliver higher charge storage density[26-28]. However, lead-based materials have the disadvantage of polluting the environment and posing a health risk to mankind[29-32]. Therefore, researchers are looking for alternative lead-free dielectric materials with higher storage efficiency. In this regard, substantial attention has been paid towards the research and development of the novel dielectric materials such as HfO_2 [33], Al_2O_3 [34], Sm_2O_3 [35], ZnO_2 [36], TiO_2 [37], Y_2O_3 and Si[38], $CaCu_2Ti_4O_{12}$ [39], CuO [40], $Ln_{2-x}Sr_xNiO_2$ [41], NiO_2 [42]. Over the past decade, substantial growth has been achieved in the progress of high-performance bulk ceramics (lead-free) dielectric materials for the storage applications of electrical energy *viz*. $SrTiO_3$, $CaTiO_3$, $BaTiO_3$, $BiFeO_3$, $AgNbO_3$ and $NaNbO_3$ based ceramics[43]. Yang *et al*. reported a lead free $SrTiO_3$ based material, $(1-x)SrTiO_3 - xBi_{0.5}(Na_{0.82}K_{0.18})Ti_{0.96}Zr_{0.02}Sn_{0.02}O_3$ where x= 0-0.5 with ϵ' 300 – 2700 and tan δ up to 0.12 in a frequency range of 1kHz to 1MHz [44]. A $NaNbO_3$ based ceramics, $0.91\,NaNbO_3 - 0.09\,Bi(Zn_{0.5}Ti_{0.5})O_3$ was developed by Y. Fan, *et al*. with relative permittivity of 700 – 1200 and

tan δ up to 0.11 in a frequency range of 1.0×10^2 Hz to 5.0×10^6 Hz[45]. A $BaTiO_3$ based ceramics stable in the frequency and temperature range of 1 – 100 Hz and 298 K - 373 K, respectively was developed by Y. Lin and group[46]. An Sm doped $AgNbO_3$ ($Sm_{0.03}Ag_{0.91}NbO_3$) was synthesized by Luo *et al.*[47] for superior energy storage. A ternary bulk ceramic containing $BiFeO_3 - BaTiO_3 - SrTiO_3$ with ϵ' 300 – 2000 and tan δ up to 1.1 in a frequency range of 1kHz to 1MHz was reported for energy storage[48].

In addition to storage efficiency, effective heat dissipation of electric equipment is essential, as heat dissipation ability directly affects the device's life. It is necessary to dissipate heat produced in a local area to prevent device malfunction, poor durability, and premature failure. Application of a cooling fan or even a heat sink are common approaches to improve the efficiency of heat transfer but they lead to large volume and weight of the entire system. Thus it is highly desirable to design materials, which can afford low dielectric loss with the desired combination of high energy density and reasonable heat-dissipating behaviour.

The main objective of this work is to develop a heat dissipating material with good dielectric properties. In the present work, multi-component mixture FPN2B has been synthesized as described later and calcined at 353 K (to obtain FPN2A) and 423 K (to obtain FPN2C). A comparative study of FPN2A and FPN2B was accomplished by various thermo-analytical techniques. Out of the two, the mixture with better thermal dissipating behaviour was picked, thermally modified and then subjected to dielectric spectroscopy.

Experimental Section

Materials

Analar grade chemicals $FeSO_4\cdot7H_2O$ (assay ≥ 99%, F8263-500G) H_3PO_4 (assay ≥ 99%, 79622) NH_4OH (Merck) from Sigma-Aldrich were used for synthesis purposes. Freshly prepared double-distilled solution water was used for solution preparation. All glass distillation system with alkaline $KMnO_4$ was used for the second distillation.

Synthesis

The required amount of $FeSO_4\cdot7H_2O$ was dissolved in double-distilled water. Thereafter, H_3PO_4 was added to the resultant solution in a 1:1 molar ratio and continuously stirred at RT for 48 hrs on a magnetic stirrer. Ammonia solution (NH_4OH) was used for neutralisation and the *p*H was maintained between 7-8. The neutralised solution was kept undisturbed for 24 hrs. After that, the precipitate was vacuum filtered and washed a few times by double distilled water tailed by ethanol. Then, in a desiccator half of the precipitate was dried over silica gel and named as FPN2B (non-calcined) mixture. The remaining half of the precipitate was calcined in an air atmosphere at 353 K for 6 h and named as FPN2A (calcined) mixture.

Instrumentation

For characterization of the above mixtures (FPN2A and FPN2B), Fourier Transform Infrared Spectroscopy (FT-IR), X-Ray Diffraction (XRD), Scanning Electron Microscope (SEM), Ultraviolet-Visible-near-IR Spectroscopy (UV-VIS-NIR), Inductively coupled plasma - optical emission spectrometry (ICP-OES), Elemental analysis Carbon, Hydrogen, Nitrogen, Sulphur (C, H, N, S), Thermogravimetry-Differential Thermal Analysis (TG-DTA), and Differential Scanning Calorimetry (DSC) techniques were used. The infrared (IR) spectra of the mixtures at RT were collected using a Thermo Nicolet Nexus 670 instrument. Inductively coupled plasma Optical Emission Spectrophotometer (ICP-OES) using iCAP-6500 DUO ICP-OES Thermo Scientific equipment was used to determine elements like Fe and P. For elemental analysis, each mixture was dissolved in 10 mL HNO_3 at 30% (v/v) and the volume was made up to 100 mL using HPLC (high-performance liquid chromatography) grade water. FLASH EA 1112 series C–H–N-S analyser was used for the determination of sulphur, nitrogen, and hydrogen percentage. All DSC measurements were carried out in a normal atmosphere in an aluminium crucible at a heating rate of 10 K min^{-1} using DSC Discovery 250 equipment. Thermogravimetric (TG) and differential thermal analysis (DTA) of all mixtures in the temperature range of 298 K to 1565 K were performed using an alumina crucible in a normal atmosphere by a TAQ600 thermal analyser. For X-ray diffraction (XRD) analysis, a PANalytical Empyrean XRD was used. Bruker AXS D8 Advance was used to find out the FWHM (full width at half maximum) of the peaks for the mixtures. The optical properties of the mixtures were studied by a Varian Cary 5000 spectrophotometer in an ultraviolet-visible–near-infrared (UV-Vis-NIR) region ranging

from 229 nm to 2500 nm. The morphology of the samples was analysed by using a FESEM (field emission scanning electron microscopy), JEOL JSM-7610F microscope. All the characterizations were carried out in SAIF-CUSAT, Kerala, and CSIR-IICT, Hyderabad.

Results and Discussion

Structural analysis

XRD and FT-IR analyses were used to characterise the structural properties of FPN2A and FPN2B. Fig. 1 manifests the FT-IR spectra of both FPN2A and FPN2B. The stretching vibration of the hydroxyl group (O–H stretching) is represented by vibrational bands at 3480 cm^{-1} in both the mixtures. The band around 3170 cm^{-1} is attributed to the asymmetric stretching vibration of N–H group. The bending mode of N-H group (narrowband) is assigned around 1400 cm^{-1}. The asymmetric stretching vibration of PO_4^{3-} ion was observed at 1045 cm^{-1}. One-shoulder peak is observed around 815 cm^{-1}, owing to the symmetric stretching of PO_4^{3-} . The bending mode of PO_4^{3-} is assigned to band near 545 cm^{-1}. The vibrational band near 480 cm^{-1} is assigned to the ν_2 modes of PO_4^{3-} ion. These vibrational bands are ascribed according to published literature[49-54]. Table-S1 (supplementary table) summarizes the vibrational bands of both the mixtures. Fig. 2 (a and b) depict PXRD patterns of synthesized multicomponent mixtures, FPN2A and FPN2B, along with their reference for comparison.

The PXRD results show that the diffraction pattern of FPN2A found congruous with the references pattern of $Fe_3(PO_4)_2 \cdot 4H_2O$ (96-900-9878) [55], $FePO_4 \cdot 2H_2O$ [56], $NH_4H_2PO_4$(01-078-2414) [57], $(NH_4)_2SO_4$(98-003-9035)[58]. Similarly, the PXRD pattern of FPN2B was found congruous with the references pattern of $Fe_3(PO_4)_2 \cdot 8H_2O$ (96-001-7476)[59], $FePO_4$(98-007-7817)[60], $NH_4H_2PO_4$(01-078-2414)[57] $(NH_4)_2SO_4$(98-003-9035)[58]. From the Williamson-Hall (W-H) plot (Supplementary figures Fig.S1 and Fig.S2), the crystallite size of FPN2A and FPN2B was calculated to be 66.1 nm and 79.5 nm, respectively. Phase quantification of both the mixtures are displayed in supplementary figures Fig.S3 and Fig.S4.

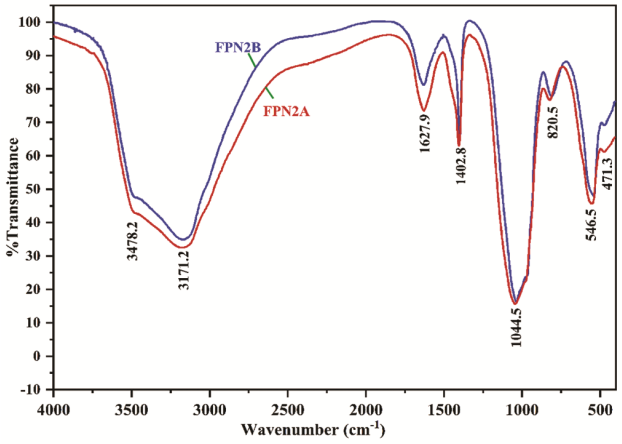

Fig. 1 — FTIR bands of FPN2A and FPN2B

Compositional analysis

Compositional analysis of both mixtures was accomplished by CHNS analysis (qualitative and quantitative) and ICP-OES (quantitative). The atomic composition of constituent elements Fe, P, Na, H, S were determined in both FPN2A and FPN2B. The chemical composition (elemental) and molecular weight of FPN2B are $0.8\,Fe_3(PO_4)_2 \cdot 8H_2O \cdot 0.8\,FePO_4 \cdot 0.5\,NH_4H_2PO_4 \cdot 0.2\,(NH_4)_2SO_4$ and 605.89 g/mol respectively. Similarly, the composition and molecular weight of FPN2A is $0.8\,Fe_3(PO_4)_2 \cdot 4H_2O \cdot 0.8\,FePO_4 \cdot 2H_2O \cdot 0.5\,NH_4H_2PO_4 \cdot 0.2\,(NH_4)_2SO_4$ and 577.06 g/mol respectively. Experimentally measured elemental atomic composition of the mixtures found consistent with theoretically calculated composition. Table 1 summarizes the measured and calculated atomic percentage of constituent elements in both mixtures.

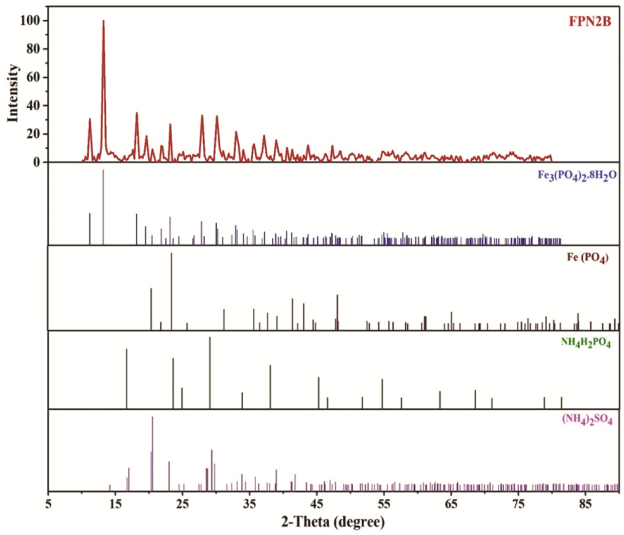

Fig. 2 — (a) PXRD pattern of FPN2A with references, (b) PXRD pattern of FPN2B with references

Table 1 — Atomic % of elements in the mixtures

S.No.	Elements (FPN2B)	Calcd (%)	Measured (%)	Elements (FPN2A)	Calcd (%)	Measured (%)
1	Fe	29.49	28.56	Fe	30.97	31.62
2	P	14.83	14.21	P	15.57	14.62
3	N	2.08	1.74	N	2.18	1.74
4	H	2.89	2.88	H	2.48	2.49
5	S	1.05	0.30	S	1.11	0.38

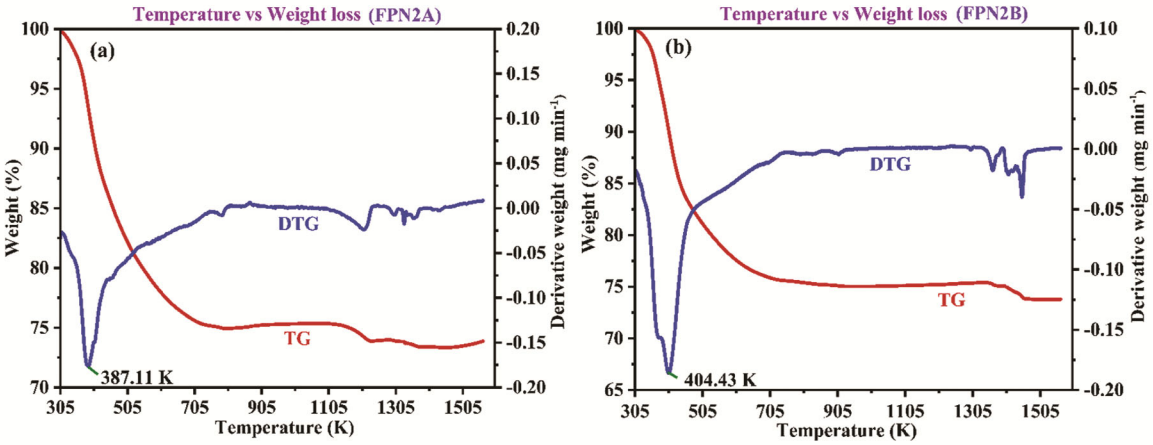

Fig. 3 — TG-DTG profiles of (a) FPN2A (b) FPN2B

Optical behaviour

UV-Vis-NIR spectra of both mixtures are manifested in Fig.S5. The absorption maxima for both FPN2A and FPN2B were found 206 nm and 208 nm respectively. The respective calculated optical bandgap of FPN2A and FPN2B are 6.02 eV and 5.96 eV which was calculated by tauc plot (Fig. S6, Fig. S7). The bandgap of FPN2A was found similar to the bandgap of AlN (6.02 eV)[61]. Refractive index (n) linkage bandgap of both FPN2A and FPN2B were calculated by moss equation[62] and found to be 1.99.

Thermal analysis

Thermal analysis was employed for both FPN2A and FPN2B to investigate the thermal stability and behaviour over a wide range of temperatures. The thermal properties of the mixtures were monitored against temperature which includes TG-DTG, DTA, and DSC analysis.

Fig. 3 manifests the TG-DTG profiles of FPN2A and FPN2B mixture.TG-DTG curve of FPN2B revealed a single step decomposition at 403.43K. The % of mass loss at 403.43K is 9.85. This corresponding mass loss is due to the removal of 3.2 mol of hydrated water from the mixture. A mass loss of 6.29% at 387.11K, was observed from TG-DTG curve of FPN2A owing to the removal of water adsorbed by the mixture while cooling post calcination.

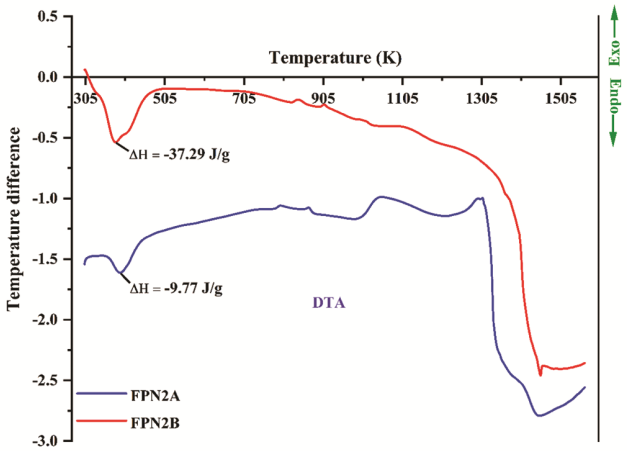

Fig. 4 — DTA curves of FPN2A and FPN2B

Fig. 4 depicts DTA curves of FPN2A and FPN2B. DTA curve of both mixtures revealed exothermic behaviour in a wide temperature range. Change in enthalpy for FPN2A is –9.77 J/g and for FPN2B is –37.29 J/g.DSC curves of FPN2A and FPN2B are displayed in Fig. 5.

In an air atmosphere, both mixtures were heated from 297.95K to 770.86K at a heating rate of 10

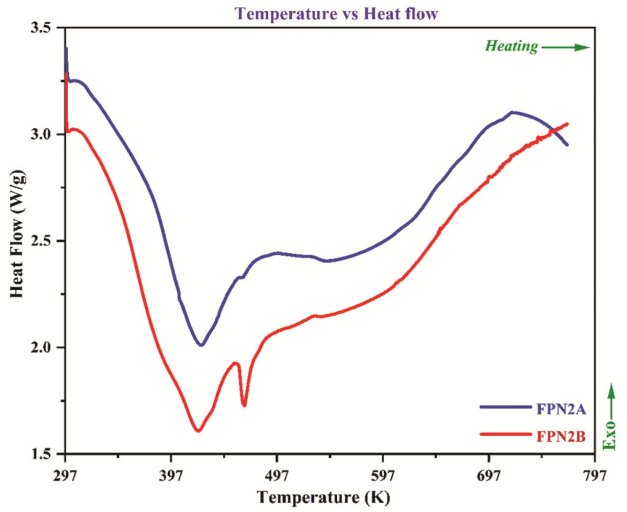

Fig. 5 — DSC curves of FPN2A and FPN2B

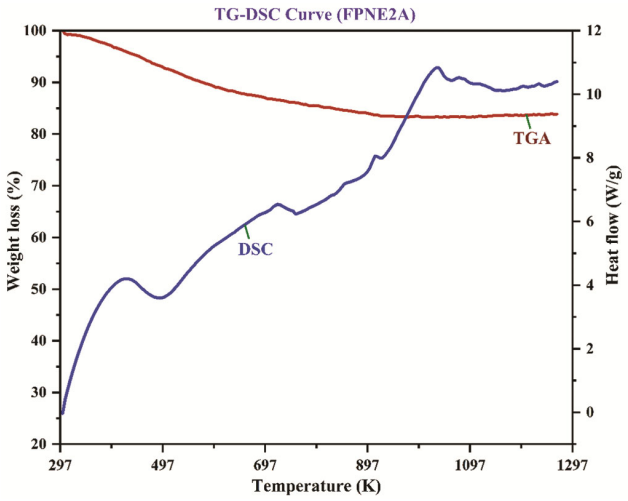

Fig. 6 — TG-DSC curve of FPN2C

K/min. Both mixtures were found exothermic throughout the whole heating cycle. The specific heat capacity of FPN2A and FPN2B were found to be 0.71 $Jg^{-1}K^{-1}$ and 0.66 $Jg^{-1}K^{-1}$. Hence, both mixtures can be used as heat-dissipating materials. The Cp values (where, Cp = heat flow / heating rate) were determined by using well known sapphire method. A blank aluminium crucible followed by sapphire were run in the same method as the sample, following which both the sapphire and sample were blank subtracted. Then, Cp value was calculated from the resultant curve using the software package available with the instrument.

A low positive C_P of 0.37 $Jg^{-1}K^{-1}$ and 0.04 $Jg^{-1}K^{-1}$ was observed for FPN2B and FPN2A respectively at ~410 K. This low C_P values correspond to the mass loss observed in TGA. It is worth mentioning here that an anomalous Cp value is observed in certain exceptional case, when a thermal event is accompanied by mass[63,64].

From the TG-DTG result, it was observed that only one decomposition step occurred at 404.43 K in FPN2B mixture. But to make the material amenable to high temperature applications, it was calcined at 423 K for 5 hrs after synthesis and the resultant mixture, FPN2C was obtained. The particle size of FPN2C was found to be 89.9 nm (Fig. S8). Again, a combined TG-DSC (Fig. 6) analysis was performed for FPN2C to study the thermal stability and properties.

No thermal decomposition was observed in the wide temperature range of (297 - 1267K) except drying of adsorbed water molecules by the mixture. DSC analysis revealed the exothermic behaviour of the mixture with a net specific heat capacity of 0.62 $Jg^{-1}K^{-1}$.

Thermal investigation revealed that the FPN2C mixture is stable across a wide temperature range and exhibits exothermic behaviour on heating. As a result, at higher temperatures, this mixture can be employed as a heat-dissipating material.

Thermal behaviour

For all mixtures, specific heat was found positive. In DSC, these mixtures were subjected to a heating cycle. So, the positive specific heat can be explained by considering a system coupling with a heat bath. These phenomena were studied for both coupled and uncoupled systems in terms of partition function[63-67].

Let us consider these mixtures as particle oscillators. Say mixtures are contained in a system 'S' and coupled by a heat bath 'B' (Fig. S9). To obtain a well-defined partition, function its motion restricted to a region.

The partition function is given by

$$Z = \frac{1}{2\sin h\left(\frac{\hbar\beta\omega}{2}\right)} \quad ...(1)$$

Where $\omega = \left(\frac{f}{M}\right)^{\frac{1}{2}}$, is frequency

$\beta = \frac{1}{K_B T}$, is inverse temperature

Specific heat capacity can be calculated by relation [63]

$$C = K_B\beta^2 \frac{\partial^2}{\partial\beta^2}\ln(Z) \quad ...(2)$$

By substituting equation 1 in equation2

$$C = K_B g\left(\frac{\hbar\beta\omega}{2}\right) \quad ...(3)$$

Specific heat capacity of the system

$$C_S = K_B g\left(\frac{\hbar\beta\omega}{2}\right) \quad ...(4)$$

Specific heat capacity of system coupled with heat bath

$$C_{SB} = K_B g\left(\frac{\hbar\beta\omega_0}{2}\right) \quad ...(5)$$

Where ω_0, is frequency because of escalation of heating at a rate of 10 K/min
Specific heat capacity of system coupling with heat bath

$$C = C_{SB} - C_B \quad ...(6)$$

$$C = K_B g\left(\frac{\hbar\beta\omega_0}{2}\right) - K_B g\left(\frac{\hbar\beta\omega}{2}\right) \quad ...(7)$$

ω_0 is significantly larger than ω because of heating. As $\omega_0 > \omega$, the specific heat capacity in the above case will be positive.

Morphology

The morphology of both mixtures was analysed by scanning electron microscope analysis. Fig. 7 manifests SEM images of FPN2A and FPN2B. Morphology of all the mixtures exhibit a hail flake laden surface appearance.

Stoichiometric calculation

The homogeneous solution containing H_3PO_4 and $FeSO_4{\cdot}7H_2O$ in a 1:1 molar ratio was neutralised by ammonia solution. The neutralization reaction occurs as follows

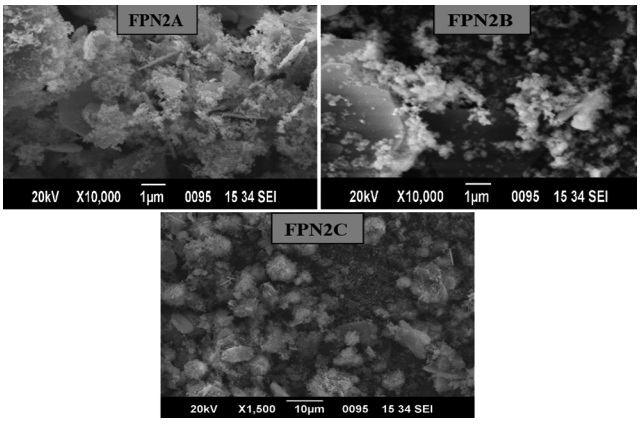

Fig. 7 — SEM images of FPN2A, FPN2B and FPN2C

$$4FeSO_4.7H_2O + 4H_3PO_4 \rightarrow Fe_3(PO_4)_2.8H_2O + FePO_4 + PO_4^{3-} + 4SO_4^{2-} + 12H^+ + 20H_2O \quad ...(8)$$

$$PO_4^{3-} + 4SO_4^{2-} + 12H^+ + 20H_2O + 9NH_4OH \rightarrow NH_4H_2PO_4 + 4(NH_4)_2SO_4 + H^+ + 29H_2O \quad ...(9)$$

As $(NH_4)_2SO_4$ is highly soluble in water 3.8 mol of $(NH_4)_2SO_4$ washed out from the mixture during the filtration process[68]. Phosphates of irons are poorly soluble in water[69,70]. The mixture was washed with deionized water and then ethanol resulting in the removal of 0.2 moles of both Fe^{II} and Fe^{III} phosphates. Due to the removal of $(NH_4)_2SO_4$ and iron phosphate the final composition of the mixture is $0.8\,Fe_3(PO_4)_2 8H_2O \cdot 0.8\,FePO_4 \cdot 0.5\,NH_4H_2PO_4 \cdot 0.2(NH_4)_2SO_4$. FPN2A was obtained by the calcination of FPN2B at 353 K in an air atmosphere. While cooling the mixture absorbed moisture from atmosphere and converted it into $0.8\,Fe_3(PO_4)_2.4H_2O \cdot 0.8\,FePO_4.2H_2O \cdot 0.5\,NH_4H_2PO_4 \cdot 0.2(NH_4)_2SO_4$. Composition of both FPN2A and FPN2B was confirmed by elemental and thermal analysis.

Dielectric properties

The dielectric properties of the mixture were measured at different temperatures by keeping the mixture at their respective temperature. The hydrated form of ferric phosphate of the mixture did not interfere during this measurement. The hydrated ferric phosphate is dehydrated during attending that temperature. This is confirmed from the TG analysis. The temperature-frequency dependent dielectric properties of the sample, FPN2C was recorded from 303 K to 573 K with a varied frequency range of 1.0×10^3 Hz to 4.0×10^6 Hz (common high-frequency range) for electrical characterization. It is well known that the dielectric properties of the sample can be studied by determining the electric parameters like real (ϵ') and imaginary permittivity (ϵ''), dielectric loss (tan δ), ac-conductivity (σ_{ac})[71]. Fig. 8 displays the frequency dispersion of dielectric constant (K) at various temperature from 303K to 573K for the sample.

It can be seen that as the frequency increases, the 'K' value decreases. It exhibits dispersion at low frequencies and then becomes constant at higher frequencies, which can be explained using space charge polarisation[72,73]. At lower frequencies, space charge polarisation dominates, and the dielectric behaviour can be explained using the Maxwell-

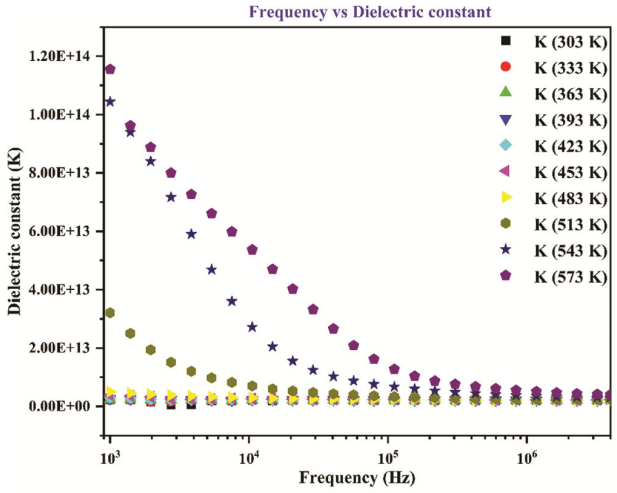

Fig. 8 — Variation of dielectric constant against frequency at various temperature

Wagner dielectric dispersion theory[74,75]. It is also worth mentioning here that there is a minor effect of frequency on dielectric constant up to 483 K, followed by a considerable increase in 'K' as temperature rises. Analogous trend in variation of dielectric constnat has been reported in other multicomponent motifs[76].

When a material is exposed to an electric field, some of the energy is stored in the material and some of the energy is dissipated in the form of heat. The real part of the permittivity (ϵ') can be used to evaluate the amount of energy stored, whereas the imaginary part (ϵ'') reflects energy dissipation.

The amount of energy stored in FPN2C when an electric field is applied can be estimated using

$$\epsilon' = \frac{Cd}{A\epsilon_0} \qquad ...(10)$$

C is capacitance, d is thickness, A ($= \pi r^2$) is the surface area of the pellet, ϵ_0 permittivity of the free space (8.85×10^{-12} Fm^{-1}). Fig. 9 and Fig. 10 display the variation of ϵ' and ϵ'' at various temperatures in a frequency range of 1.0×10^3 Hz to 4.0×10^3 Hz for FPN2C. Fig. 9 shows that ϵ' has a slight variation of ~17-19 over a wide range of frequency upto 483 K and after that attend higher values of 1000 at lower frequencies and steadily decreases as frequency increases.

This dielectric behaviour can be explained based on maxwell-wagner model and koops theory . At lower frequencies, it can be seen that ϵ' increases as the temperature rises, but it is temperature independent at higher frequencies. The dissipation

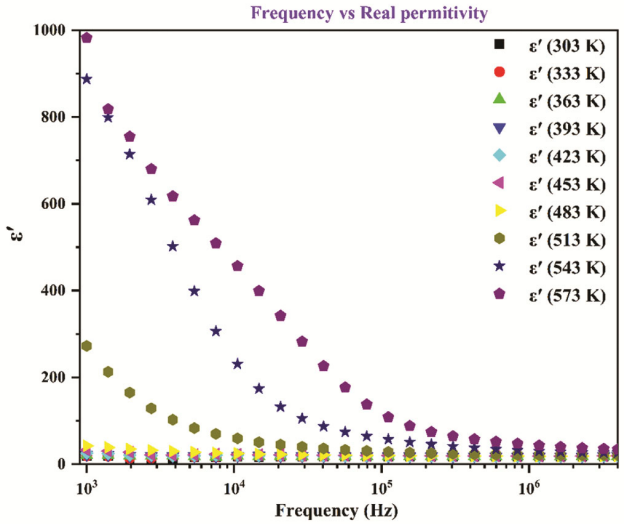

Fig. 9 — Variation of real permittivity against frequency at various temperature

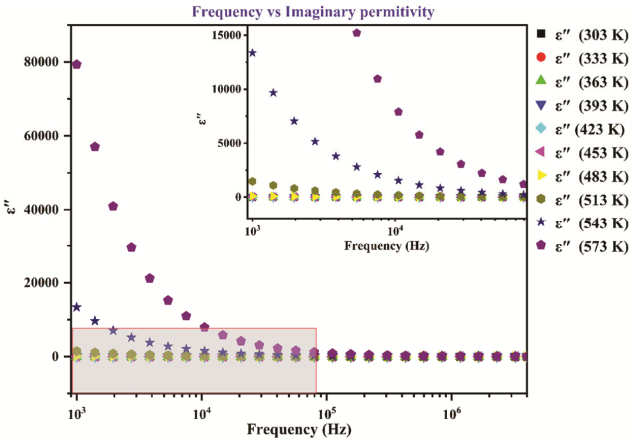

Fig. 10 — Variation of dissipation factor against frequency at various temperature

factor (Fig. 10) shows a similar trend as that of the dielectric constant.

The value of ϵ'' is high at low frequencies for 543 K and 573 K, but as the frequency increases, the value gradually decreases and becomes very small. The temperature also has an effect on ϵ'', in addition to frequency, there is a minor increase in ϵ'' up to 513 K, but after that, the dissipation factor increased significantly. The entire dielectric loss in a material can be calculated using the loss tangent (tan δ), which is given as below[77]

$$\tan\delta = \frac{\epsilon''}{\epsilon'} \qquad ...(11)$$

The dissipation factor (ϵ'') has a significant impact on dielectric loss, as shown in equation 11. The

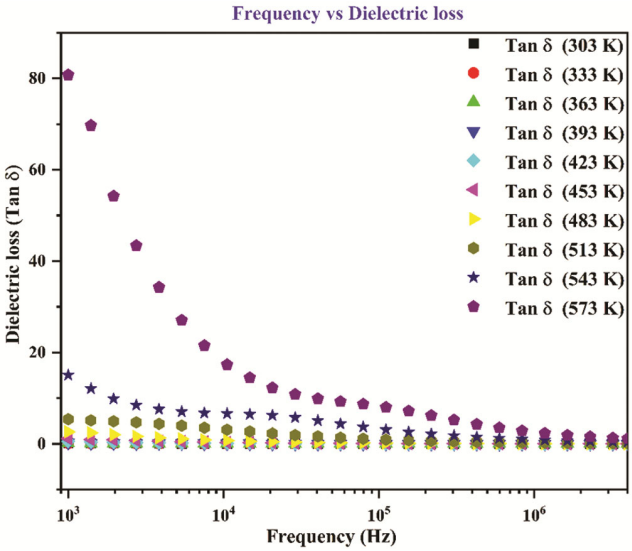

Fig. 11 — Variation of dielectric loss against frequency at various temperature

dielectric loss of a material depends on synthesis procedure, composition, structure of the material, and temperature. In Fig. 11, the dielectric loss of FPN2C is shown against frequency from 1.0×10^3 Hz to 4.0×10^3 Hz at various temperatures.

The variation of dielectric loss with frequency shows a similar trend as that of the dissipation factor. A very small ' tan δ ' of ~0.04 - 0.08 is observed in the whole frequency range up to 453 K. At low frequency, ' tan δ ' is large and then subsequently decreases as frequency increases. The high value of ' tan δ ' at lower frequency corresponds to high value of resistivity[78]. The decreasing values of 'tan δ' are attributed to prohibiting of charge carriers[79]. The ' tan δ ', on the other hand, is found to increase when the temperature goes up. The dielectric loss is found to be minimal up to 543 K, but attained maximum at 573 K.

AC-conductivity

Frequency dependant ac-conductivity of FPN2C can be determined from dielectric data by using equation 10 [77]

$$\sigma_{ac} = \epsilon' \epsilon_0 \omega \tan\delta \quad ...(12)$$

ω (= $2\pi f$) is angular frequency, ϵ' is real part of the permittivity, ϵ_0 permittivity of free space, tan δ is dielectric loss.

Fig. 12 manifests the variation of ac-conductivity of FPN2C with temperature at various frequencies. As the temperature increases 'σ_{ac}' is found to be constant up to 483 K and then increases with further increase

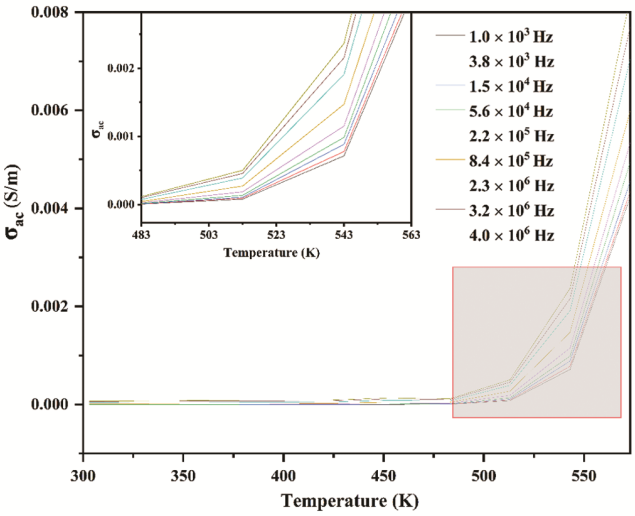

Fig. 12 — Variation of AC conductivity with temperature

in temperature above 450K. Furthermore, 'σ_{ac}' is increased with increase in frequency which can be described by hopping of charge carriers more frequently with increasing frequency[80]. The 'σ_{ac}' shows that resistivity of the material is so high that they are almost temperature independent from 303 K to 483 K. The high resistivity of FPN2C revealed the insulating property. After 483 K, conductivity of the sample increased up to measured temperature range. The increase in 'σ_{ac}' can be explained by the fact that it is a consequence of thermally activated process which can be described by Arrhenius relation

$$\sigma_{ac} = \sigma_o \left(-\frac{E_a}{KT}\right) \quad ...(13)$$

σ_o is pre-exponential factor, E_a is activation energy, K is Boltzmann constant

Conclusions

In summary, synthesis of multicomponent mixture FPN2B and its calcined mixtures FPN2A (353 K) and FPN2C (423 K) have been reported. Thermal analysis revealed heat dissipating behaviour of the mixtures. TGA revealed thermal stability of FPN2C over a wide range of temperature. For FPN2C, a slight variation is observed in dielectric constant and dielectric loss over a wide range of frequency (1.0×10^3 Hz to 4.0×10^3 Hz) upto 483 K. The 'σ_{ac}' for FPN2C is found to be 8.96×10^{-8} S/m upto 483 K. Further, a notable 'tan δ' value of 0.04 – 0.08 is observed upto 453 K. Such dielectric materials with a good thermal stability and heat dissipating behaviour can be used in fabricating selective electrical appliances to reduce their overheating related damage.

Funding

The authors declare that no funds, grants, or other support were received during the preparation of this manuscript.

Conflict of Interest

The authors have no relevant financial or non-financial interests to disclose.

Supplementary Information

Supplementary information is available in the website http://nopr.niscpr.res.in/handle/123456789/58776. Should any raw data files be needed in another format they are available from the corresponding author upon reasonable request.

Author Contributions

All authors contributed to the study conception and design. Material preparation, data collection and analysis were performed by Akash Kumar Sahu, Suprava Nayak and Gouri Sankhar Brahma. The first draft of the manuscript was written by Suprava Nayak and all authors commented on previous versions of the manuscript. All authors read and approved the final manuscript.

Acknowledgement

The authors would like to thank the Department of Chemistry, IFHE University, Hyderabad and G. M. University, Sambalpur for financial support. SN is thankful to GM University for allowing her to get associated with this project.

References

1 Yao Z, Song Z, Hao H, Yu Z, Cao M, Zhang S, Lanagan M T & Liu H, *Adv Mat*, 29 (2017) 1601727.
2 Chen X, Han X & Shen Q D, *Adv Electronic Mat*, 3 (2017) 1600460.
3 Li Q, Chen L, Gadinski M. R, Zhang S, Zhang G, Li H U & Wang Q, *Nature*, 523 (2015) 576.
4 Khanchaitit P, Han K, Gadinski M R, Li Q & Wang Q, *Nature Comm*, 4 (2013) 1.
5 Whittingham M S, *Mrs Bulletin,* 33 (2008) 411.
6 Thakur V K & Gupta R K, *Chem Rev,* 116 (2016) 4260.
7 Luo X, Wang J, Dooner M & Clarke J, *Applied energy,* 2015, 137 (2015) 511.
8 Kang B & Ceder G. *Nature*, 458 (2009) 190,
9 Tang H, Lin Y & Sodano H A, *Adv Energy Mat*, 3 (2013) 451.
10 Pandya S, Wilbur J, Kim J, Gao R, Dasgupta A, Dames C & Martin L W, *Nature Mat*, 17 (2018) 432.
11 Dunn B, Kamath H & Tarascon J M, *Science*, 334 (2011) 928.
12 Chu B, Zhou X, Ren K, Neese B, Lin M, Wang Q & Zhang Q, *Science*, 313 (2006), 334.
13 Ibrahim H, Ilinca A & Perron J. *Renewable & Sustainable Energy Rev*, 12 (2008) 1221.
14 Luo H, Zhou X, Ellingford C, Zhang Y, Chen S, Zhou K & Wan C, *Chem Soc Rev*, 48 (2019) 4424.
15 Kornbluh R D, Pelrine R, Prahlad H, Wong-Foy A, McCoy B, Kim S & Low T, *MRS Bulletin*, 37 (2012) 246.
16 Chen D & Pei Q, *Chem Rev*, 117 (2017) 11239.
17 Perju E, Shova S & Opris D M, *ACS App Mat Interfaces*, 12 (2020) 23432.
18 Zhang Q M & Serpe M J, *Chem Phys Chem*, 18 (2017) 1451.
19 Ji X, Liu X, Cacucciolo V, Imboden M, Civet Y, El Haitami A, & Shea H, *Science Robotics*, 4 (2019) eaaz6451.
20 Bauer S, Bauer-Gogonea S, Graz I, Kaltenbrunner M, Keplinger C & Schwödiauer R, *Adv Mat*, 26 (2014) 149.
21 Kellaris N, Venkata V G, Rothemund P & Keplinger C, *Extreme Mechanics Letters*, 29 (2019) 100449.
22 Qiu Y, Zhang E, Plamthottam R & Pei Q, *Accounts Chem Res*, 52 (2019) 316.
23 Kornbluh R D, Pelrine R & Pei Q, *Int Soc Optics & Photonics*, 4698 (2002) 254.
24 Kaltenbrunner M & Bauer S, *Stretchable Electronics* 2012, 287-303. DOI:10.1002/9783527646982
25 Lopez J, Mackanic D G, Cui Y & Bao Z, *Nature Rev Mat*, 4 (2019) 312.
26 Hao X, Wang Y, Yang J, An S & Xu J, *J App Phy*, 112 (2012) 114111.
27 Zhang Q, Dan Y, Chen J, Lu Y, Yang T, Yao X & He Y, *Ceramics Int*, 43 (2017) 11428.
28 Wang X, Zhang L, Hao X & An S, *Mat Research Bulletin*, 65 (2015) 73.
29 Yu Z, Liu Y, Shen M, Qian H, Li F & Lyu Y, *Ceramics Int*, 43 (2017) 7653.
30 Li Q, Zhou C, Xu J, Yang L, Zhang X, Zeng W & Rao G, *J Mat Science: Mat in Ele*, 27 (2016) 10810.
31 Xu N, Liu Y, Yu Z, Yao R, Ye J & Lu Y, *J Mat Sci: Mat Ele*, 27 (2016) 12479.
32 Yuan C, Meng L, Liu Y, Zhou C, Chen G, Feng Q & Rao G, *J Mat Sci Mat Ele*, 26 (2015) 8793.
33 Park I S, Lee T, Ko H & Ahn J, *J Korean Phy Soc*, *49* (2006) S760.
34 Mahajan A M, Khairnar A G & Thibeault B J, *Semiconductors*, 48 (2014) 497.
35 Kaya S, Yilmaz E, Kahraman A Y S E G Ü L & Karacali H, *Nuclear Inst Meth Phy Res Sec B: Beam Inter Mat & Atoms*, 358 (2015) 188.
36 Zhu J & Liu Z G, *App Phy A*, 78 (2004) 741.
37 Paily R, Das Gupta A, Dasgupta N, Bhattacharya N, Misra P, Ganguli T & Tyagi A K, *Applied Surface Sci*, 187 (2002) 297.
38 Boukerika A & Guerbous L, *J luminescence*, 145 (2014) 148.
39 Subramanian M A, Li D, Duan N, Reisner B A & Sleight A W,. *J Solid-State Chem*, 151 (2000) 323.
40 Thongbai P, Maensiri S & Yamwong T, *J Applied Phy*, 104 (2008) 036107.
41 Wang J, Liu G, Jia B W, Liu X Q & Chen X M, *Ceramics Int*, 40 (2014) 5583.

42 Wu J, Nan C W, Lin Y & Deng Y, *Phy Rev Lett*, 89 (2002) 217601.
43 Yang Z, Du H, Jin L & Poelman D, *J Mat Chem A*, 9 (2021), 18026.
44 Yang H, Yan F, Lin Y & Wang T, *J Alloys Comp*, 728 (2017) 780.
45 Fan Y, Zhou Z, Liang R & Dong X, *J Eur Ceramic Soc*, 39 (2019) 4770.
46 Lin Y, Li D, Zhang M, Zhan S, Yang Y, Yang H & Yuan Q, *ACS Applied Mat Interfaces*, *11* (2019) 36824.
47 Luo N, Han K, Zhuo F, Xu C, Zhang G, Liu L & Wei Y, *J Mat Chem A*, 7 (2019) 14118.
48 Sun Y, Liu H, Liu F & Liu G, *J Mat Sci Mat Ele*, 32 (2021) 21188.
49 Liu Y, Li Z, You Y, Zheng X & Wen J, *RSC Adv*, 7 (2017) 51281.
50 Frost R L, Martens W, Williams P A & Kloprogge J T, *Mineralogical Magazine*, 66 (2002) 1063.
51 Frost R L, Xi Y, Scholz R, Belotti F M & Filho M C, *Spectroscopy Lett*, 46 (2013) 415.
52 Samala S, Brahma G S & Swain T, *Monatshefte für Chemie-Chem Monthly*, 151 (2020) 141.
53 Sahu A K, Aravind R, Brahma G S & Swain T, *J Energy Storage,*47 (2021) 103598.
54 Sahu A K, Aravind R, Brahma G S & Swain T, *J Solar Energy Eng*, 144 (2021)1.
55 Abrahams S C & Bernstein J L, *J Chem Physics*, 44 (1966) 2223.
56 Zaghib K & Julien C M, *J Power Sources*, 142 (2005) 279.
57 Joshi J H, Joshi G M, Joshi M J, Jethva H O & Parikh K D, *New J Chem*, 42 (2018) 17227.
58 González-Silgo C, Solans X, Ruiz-Pérez C, Martínez-Sarrión M L, Mestres L & Bocanegra E, *J Phy Condensed Matt*, 9 (1997) 2657.
59 Mori H & Ito T. *Acta Crystallograp*, 3 (1950) 1.
60 Mittal R, Chaplot S L, Kolesnikov A I, Loong C K, Jayakumar O D & Kulshreshtha S K, *Phy Rev B*, 66 (17) 174304.
61 Shah A & Mahmood A, *Physica B Condensed Matt*, 407 (2012) 3987
62 Moss T S, *Phy Status Solid (b)*, 131 (1985) 415.
63 Ingold G L, Hänggi P & Talkner P, *Phy Rev E*, 79 (2009) 061105.
64 Hänggi P, Ingold G L, *Acta Phy Pol B*, 37 (2006) 1537.
65 Hänggi P, Ingold G L, Talkner P, *New J Physics*, 10 (2008) 1.
66 Leggett A J, Chakravarty S, Dorsey A T, Fisher M P A, Garg A & Zwerger W, *Rev Mod Phy*, 59 (1987) 1.
67 Rudrarapu A, Brahma G S & Swain T, *Int J Energy Res*, 45 (2021) 13911.
68 Haynes W M, *CRC H & Book Chemistry Physics,* (CRC Press) 2014.
69 Barroso C B & Nahas E, *Brazilian Archives Bio Tech*, 56 (2013) 181.
70 Priambodo R, Shih Y J & Huang Y H, *RSC Adv*, 7 (2017) 40819.
71 Goldstein J I, Newbury D E, Michael J R, Ritchie N W, Scott J H J & Joy D C, *Scanning Electron Microscopy & X-ray Microanalysis,* (Springer) 2017.
72 Shaikh A M, Bellad S S & Chougule B K *J Mag Mag Mat*, 195 (1999) 384.
73 Kambale R C, Adhate N R, Chougule B K & Kolekar Y D, *J Alloys Comp*, 491 (2010) 372.
74 Samuel M S, Koshy J, Chran A & George K C, *Current Applied Physics*, 11 (2011), 1094.
75 Samuel M S, Koshy J, Chran A & George K C, *Phy B: Condensed Matt*, 406 (2011) 3023.
76 Turky G & Dawy M, *Mat Chem Phy*, 77 (2003) 48.
77 Durrani, S. K, Naz, S, Mehmood, M, Nadeem, M& Siddique, M. *J Saudi Chem Society*, 21 (2017) 899.
78 Kadam A A, Shinde S S, Yadav S P, Patil P S & Rajpure K Y, *J Mag Mag Mat*, 329 (2013) 59.
79 Mumtaz M, Hassan M, Ali L, Ahmad Z, Imtiaz M A, Aamir M F & Nadeem K, *Applied Physics A*, 126 (2020) 1.
80 Moradmard H, Shayesteh S F, Tohidi P & Abbas Z, *J Supercond Novel Mag*, 29 (2016) 2171